Geochemistry, Geophysics, Geosystems

RESEARCH ARTICLE
10.1029/2018GC007940

The Mid-Atlantic Ridge Near 13°20′N: High-Resolution Magnetic and Bathymetry Imaging

R. C. Searle[1], C. J. MacLeod[2], C. Peirce[1], and T. J. Reston[3]

[1]Department of Earth Sciences, Durham University, Durham, UK, [2]School of Earth and Ocean Sciences, Cardiff University, Cardiff, UK, [3]School of Geography, Earth and Environmental Sciences, University of Birmingham, Birmingham, UK

Key Points:
- Crustal magnetization is heterogeneous and three-dimensional, with a narrow and discontinuous Brunhes anomaly
- Normal magnetization broadly matches the side scan sonar-derived neovolcanic zone, consistent with independent core complex evolution
- Post-anomaly-2 crustal accretion has been highly asymmetric, faster to the west (core complex side)

Supporting Information:
- Supporting Information S1

Correspondence to:
R. C. Searle,
r.c.searle@durham.ac.uk

Citation:
Searle, R. C., MacLeod, C. J., Peirce, C., & Reston, T. J. (2019). The Mid-Atlantic Ridge near 13°20′N: High-resolution magnetic and bathymetry imaging. *Geochemistry, Geophysics, Geosystems*, *20*, 295–313. https://doi.org/10.1029/2018GC007940

Received 4 SEP 2018
Accepted 19 NOV 2018
Accepted article online 21 DEC 2018
Published online 16 JAN 2019

Abstract We describe detailed magnetic and bathymetric studies around 13°N on the Mid-Atlantic Ridge, a site of extensive detachment faulting. Inversion of closely spaced sea surface magnetic anomalies reveals a disorganized pattern of magnetization, with anomalies younger than anomaly 2 being poorly delineated. The Brunhes anomaly width is highly variable but averages ~60% of that predicted for the regional spreading rate. It is often split, both along and across axis, by apparently reversely magnetized crust. Gaps in the Brunhes anomaly match gaps in the neovolcanic zone inferred from acoustic backscatter. A strong negative magnetization is associated with the oceanic core complex (OCC) at 13°20′N (OCC1320) and is inferred to arise from exhumed old, reversely magnetized lithosphere. The inferred position of the magmatic axis implies ~30% asymmetry of crustal accretion post-anomaly-2. Higher spatial resolution magnetic anomalies near the seafloor, measured by autonomous underwater vehicle, are qualitatively similar to earlier deep-towed data but differ somewhat from the sea surface magnetics. We interpret this mismatch as reflecting the differing sensitivities of the two observing geometries and the existence of a highly heterogeneous topography and magnetization. This suggests that a strongly three-dimensional structure exists, more compatible with a geodynamic model where neighboring OCCs are not connected but evolve independently. A modeled near-seafloor profile through OCC1320 shows low positive magnetization below the smooth dome. A second profile, running E-W between two OCCs, shows high magnetization coinciding with a large seamount, reflecting recent off-axis volcanism. Measured microbathymetry reveals extensive small volcanic cones on this seamount and confirms previous interpretations of OCC morphology.

Plain Language Summary Slow spreading ridges form new crust both by magma accreting onto the trailing edges of tectonic plates, or by deeper, ductile mantle being pulled up ("exhumed") and becoming rigid, in "oceanic core complexes" (OCCs): a process of "asymmetric accretion." As part of a larger study of OCCs, we made detailed measurements of seafloor topography and variations in the magnetic field at the sea surface and, while other operations were underway, at the seafloor, using a robotic submarine. Measuring topography allows us to map volcanoes and fractures, while processing and modeling magnetic field variations yield the seafloor spreading history by mapping well-dated reversals of the Earth's field. Rocks magnetized with the current north pointing polarity during the past 800,000 years have a complex pattern and form a narrower band than expected, with significant gaps and asymmetry. The western plate has been accreting almost twice as fast as the eastern plate. The topography and magnetic pattern suggest a complex interplay of accretion by volcanism and exhumation, with volcanic activity jumping from place to place, with crustal stretching along large "detachment faults" (which cut through the entire lithosphere and form OCCs) and many smaller fractures. Thus, crustal development here is thoroughly three-dimensional.

1. Introduction

The axial region of the Mid-Atlantic Ridge (MAR) between approximately 13°N and 14°N is characterized by numerous oceanic core complexes (OCCs) bounded by detachment faults, and by blocky topography with widely spaced and back-tilted normal fault blocks (Smith et al., 2006). It is thus typical of asymmetric ocean crustal accretion (Escartin et al., 2008). Previous TOBI deep-towed side scan sonar data reveal a complex pattern of tectonism and magmatism, including at least one active detachment fault (MacLeod et al., 2009). Coincident magnetic anomalies vary significantly among the 6-km-spaced TOBI track lines, suggesting extensive and variable seafloor spreading, and show the Brunhes anomaly to be significantly narrowed and apparently absent in places (Mallows & Searle, 2012). Some authors consider neighboring oceanic

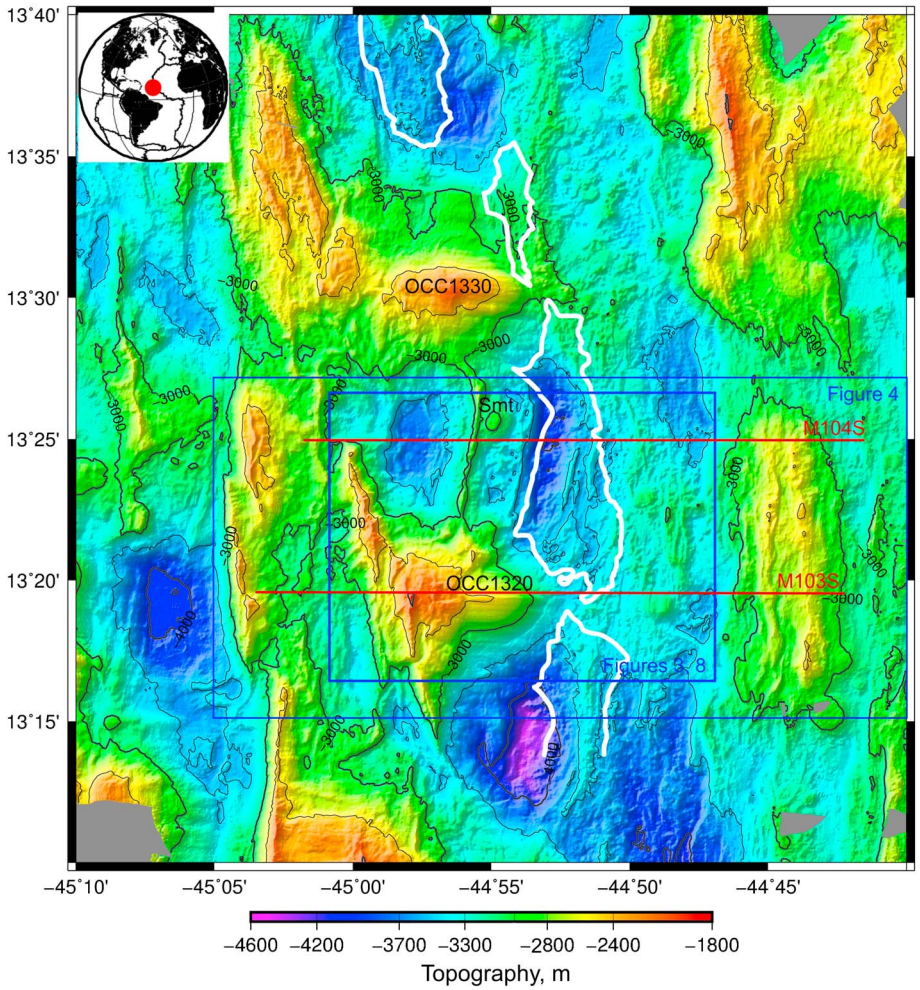

Figure 1. Bathymetry of the 13°N study area, including multibeam data from the ship-based EM120, gridded at 20-m node spacing followed by a 100-m median filter and 100-m Gaussian filter. Contours at 500-m intervals shown by fine gray lines and at 1,000-m intervals by thicker gray lines. OCC1320 and OCC1330 are annotated. "Smt" indicates the off-axis seamount referred to in text. White lines outline the neovolcanic zone after Mallows and Searle (2012). Also shown are the areas of Figures 3, 4, and 8 (blue boxes), and the locations of the modeled Autosub magnetic profiles M103S and M104S (red lines). Inset shows location of study area. OCC = oceanic core complex.

detachment faults to be essentially continuous, long-lasting features active on a segment scale that may be linked subsurface (Cann et al., 2015; Escartin et al., 2008; Reston & Ranero, 2011; Schouten et al., 2010; Smith et al., 2008). In contrast, MacLeod et al. (2009) proposed a model for independent cycles of formation, development and demise of adjacent OCCs.

In January–February 2016, we undertook a multidisciplinary geophysical campaign in this region, with the primary aim of imaging the full crust and uppermost mantle in three dimensions and at a range of resolutions, in order to test these competing models (Reston & Peirce, 2016). During seismic operations we collected closely spaced, ship-based multibeam bathymetry soundings and total magnetic field measurements. Between the seismic phases we carried out a number of dives with the autonomous underwater vehicle (AUV) Autosub 6000 (McPhail, 2009), during which we obtained high-resolution microbathymetry and near-bottom magnetic field measurements. Here we present an analysis of these data.

1.1. Study Area

Most of our near-seabed operations were conducted between 13°14′N and 13°35′N (Figures 1 and 2). The regional spreading half rate is 12.5 km/Ma (DeMets et al., 2010; Fujiwara et al., 2003), but anomalies

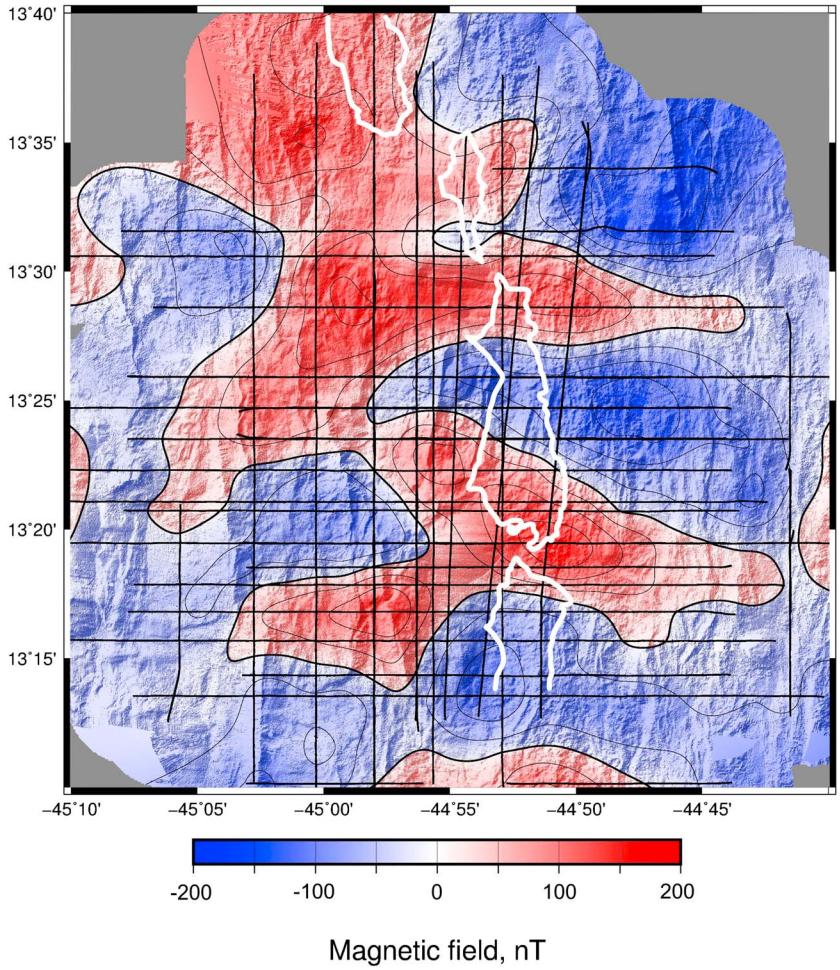

Figure 2. Total magnetic field anomaly measured at the sea surface (color) along the track lines shown in black, superimposed on the shaded bathymetry from Figure 1, illuminated from the NW. Contours are shown at 50-nT intervals, with 0 nT *in* bold. White lines outline the neovolcanic zone after Mallows and Searle (2012). Magnetic data were gridded at 0.125-km node spacing using GMT (Generic Mapping Tools) *surface* command (Wessel & Smith, 1998) and then filtered with a 1.25-km median filter.

younger than chron 2n (1.95–1.77 Ma; Cande & Kent, 1995) are poorly developed (Smith et al., 2008). The area is dominated by two OCCs. One, centered on 13°30′N (hereafter called "OCC1330"), is inferred to be failing (MacLeod et al., 2009; Mallows & Searle, 2012) or recently defunct (Escartin et al., 2017). The other, near 13°20′N (hereafter "OCC1320"), is bounded by an actively slipping detachment fault (Escartin et al., 2017; MacLeod et al., 2009; Parnell-Turner et al., 2017). The MAR "axis" lies immediately to the east of these OCCs (Figure 1).

1.2. Previous Work

The first comprehensive survey of the 13°N area measured the bathymetry, gravity, and magnetic anomaly at the sea surface on NW-SE oriented tracks spaced 9 km apart (Smith et al., 2006, 2008). That study identified the area as being characterized by "vigorous tectonic extension," with steeply rotated normal fault blocks and numerous OCCs near and off axis. Smith et al. (2006, 2008) suggested that these features were a consequence of periods of limited melt production and thus represented amagmatic crustal accretion. MacLeod et al. (2009) and Mallows and Searle (2012) carried out further geophysical work, including a detailed survey using the TOBI deep-towed instrument on 6-km-spaced E-W tracks, acquiring 30-kHz side scan sonar images and magnetic measurements ~400 m above the seafloor, in addition to sea surface gravity, magnetic and multibeam bathymetry data. Escartin et al. (2017) investigated the

two OCCs in detail, using the AUV Abyss to measure microbathymetry, Eh, and nephelometry, and the ROV Victor 6000 to obtain video and rock samples. That study revealed details of detachment fault structure, development, and denudation. Recently, Parnell-Turner et al. (2017) reported the temporal and spatial distribution of microseismicity surrounding OCC1320, acquired during a 6-month passive ocean bottom seismograph deployment (Peirce, 2014a, 2014b), that revealed a pattern of both compressional and extensional focal mechanisms associated with the detachment footwall and its rotation during progressive exhumation.

2. Data Acquisition

2.1. Ship-Borne Measurements

We revisited the 13°N area during RRS James Cook cruise JC132 in January–February 2016 (Reston & Peirce, 2016). The ship was equipped with an EM120 multibeam echosounder and Micro-G Lacoste-Romberg air-sea gravimeter, which were operated continuously throughout the cruise. The EM120 data (Figure 1) were sufficiently dense to allow gridding at up to 10-m spacing. A SeaSpy proton precession magnetometer was towed in the near surface behind the ship during seismic operations, along a grid of N-S and E-W tracks with an average spacing of ~3 km (Figure 2). Ship positioning was by GPS. Magnetic data were corrected for position of the sensor behind the ship, and IGRF version 12 was removed (Erwan et al., 2015). The gridded total field anomaly is shown in Figure 2.

2.2. *Autosub* Acquisition

Opportunistically, between seismic operations we deployed and recovered the AUV Autosub 6000 for ten ~24-hr-long, near-seafloor transects. Figure 3 shows tracks along which microbathymetry was obtained, and Figure 4 shows dives (labeled) that collected magnetic data. Autosub position at each launch and recovery was set from the ship's GPS, complemented by short-baseline acoustic navigation from the ship, with along-track position estimated by tracking the sea floor with an acoustic Doppler current meter. Autosub was programed to track the seabed at a set height of 150 m for dives M103 and M104, 120 m for M105 to M109, and 115 m for dives M110 to M112, the variation resulting from attempts to find a height that enabled the vehicle to maintain a stable seabed lock. In practice, the Doppler current meter frequently lost track of the bottom, resulting in degradation of positional accuracy. Comparison of vehicle depth and water depth profiles suggests positions may have been in error by up to at least 1.6 km. Moreover, the vehicle altitude increased to as much as 600 m in places, with the vehicle losing its way at changes in course, resulting in multiple circles above the same location before proceeding along its programed track.

2.2.1. Autosub Bathymetry

Autosub carried an EM2040 multibeam echosounder but this only worked during dives M103 (partially) and M107–M112 (Figure 3 inset). Vehicle tracks were adjusted to match (by eye) features visible in the EM120 bathymetry and the adjusted data were gridded to 4-m resolution. These data were then combined with the EM120 and Abyss microbathymetry from the 2013 French ODEMAR expedition, supplied courtesy of J. Escartin (Figure 3). No correction was made for ocean tides or other offsets between the data sets.

2.2.2. Autosub Magnetics

Autosub was also equipped with an Applied Physics Systems model 1540 triaxial fluxgate magnetometer mounted in the vehicle nose. It was run continuously during all dives (Figure 4). “Figure-of-eight” calibration turns were made before and after each dive, but postdive analysis showed that insufficient pitching had been used to match the full dive conditions, where vehicle pitch commonly ranged between −8° (nose down) and +18° (nose up) as the vehicle traversed the rough MAR terrain (supporting information Figures S1a and S1b). We corrected the data from each dive as follows:

i The three-component data were converted to total field.
ii A heading correction was obtained and applied by fitting a sine function to all total field data from each dive separately.
iii We sought areas where field measurements and pitch were well correlated (e.g., supporting information Figure S1b) and fitted a polynomial to these. An order 2 polynomial (supporting information Figure S1c) was sufficient to remove virtually all pitch effects (supporting information Figure S1d). Vehicle roll was negligible and was not corrected.

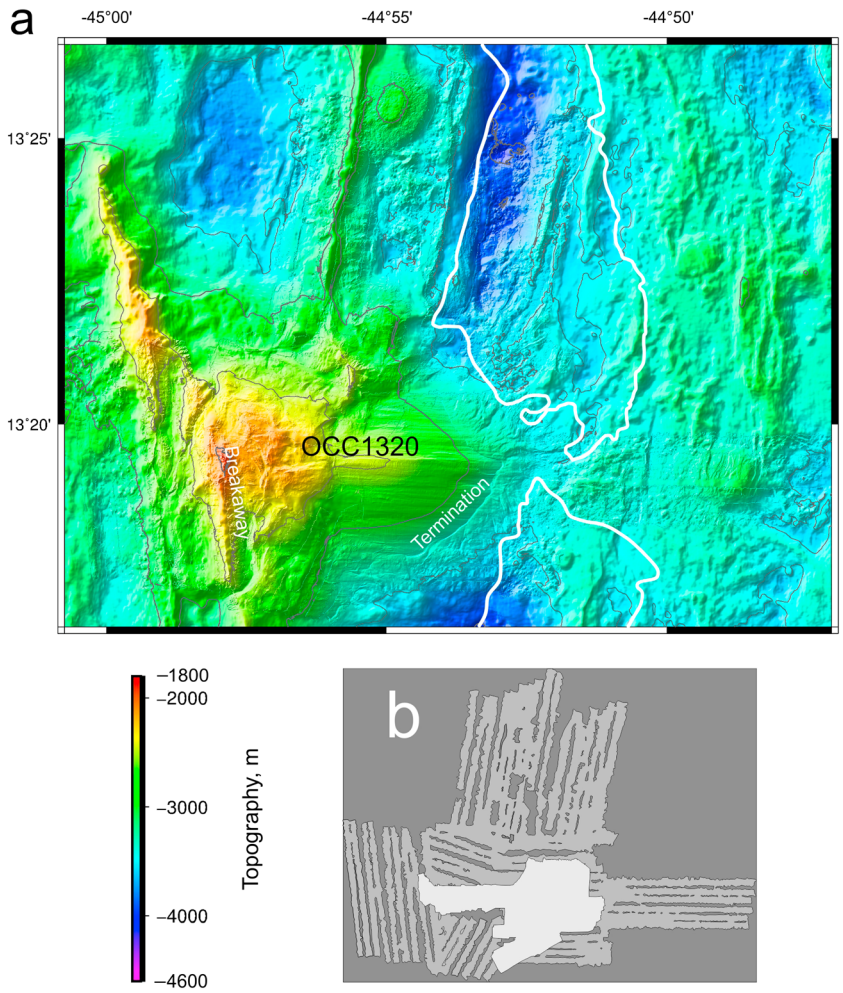

Figure 3. (a) EM120, Autosub and Abyss multibeam data combined with preference to highest-resolution data (Abyss > Autosub > EM120) and regridded at 4-m spacing. Thick dark lines are the 2,000- and 3,000-m contours; thin dark lines are all other contours at 500 m intervals. White lines outline neovolcanic zone after Mallows and Searle (2012). (b) Data coverage with shipboard EM120 in dark gray, Autosub EM2040 in midgray, and Abyss Reson 7125 in light gray.

iv On a number of dives there were a few instantaneous jumps in the field value. Some of these correlated with the EM2040 switching on or off, but others are unaccounted for. We corrected them by adding an appropriate constant value to all measurements following the jump.
v Finally, we removed the mean field value for each dive to create a relative anomaly.

3. Modeling

We carried out a standard inversion of the sea surface magnetic anomaly to crustal magnetization (Parker & Huestis, 1974) using the topography shown in Figure 1; the result is shown in Figure 5. This inversion assumes a magnetic source layer 0.5 km thick whose top is coincident with the seafloor and magnetization in the direction of a geocentric axial dipole (declination 0°, inclination 25.6°). The amplitude of the magnetization solution scales approximately inversely with the source layer thickness. For example, increasing the thickness to 1 km reduces magnetization by a factor of about 2, without significantly changing the shape. The annihilator, which is the magnetization distribution that produces zero anomaly and thus can be added to the solution in arbitrary quantity, ranges from 0.59 to 1.50 A/m (supporting information Figure S2). Addition of more than one annihilator shifts the average magnetization well away from zero, and the overall shape of the magnetization solution is not changed. Consequently, no annihilator has been added in

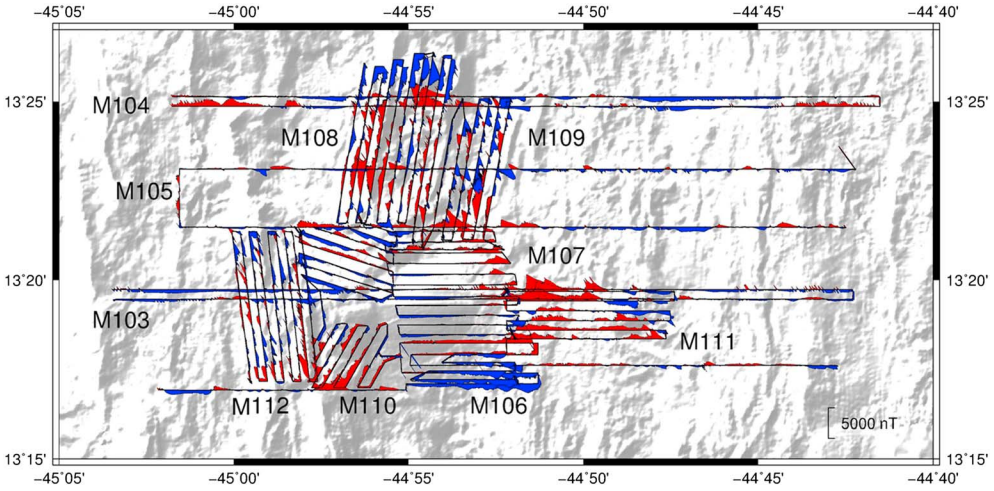

Figure 4. Total magnetic field anomaly derived from Autosub 6000 near-seabed measurements, plotted along preprogramed tracks and superimposed on the shaded bathymetry from Figure 1, illuminated from the NW. Positive anomalies are plotted along azimuth 315° and shaded red, negative anomalies along 135°, shaded blue. Scale bar at lower right. "M" numbers identify individual dives. Profiles M103S and M104S are shown in detail in Figures 6 and 7. See text for details of data processing.

Figure 5. This inversion result is compatible with those of Smith et al. (2008) and Mallows and Searle (2012) and is now confirmed to a horizontal resolution of ~3 km.

We forward modeled two of the long E-W Autosub profiles: M104S (the southernmost of the pair of M104 lines) and M103S (the southernmost of the M103 pair). All other Autosub profiles lack the necessary precision in navigation or altitude to permit modeling. We chose to forward model rather than invert the anomalies in order to maintain a high spatial resolution, since inversion has to be carried out at or above the minimum depth along the profile. In the 13°N case, this would be at less than 2 km water depth, (similar to the previous TOBI study), while the axial valley floor is deeper than 3,500 m. Consequently, inversion would negate much of the high resolution gained by deploying the magnetometer near the seafloor.

Because the Autosub altimeter frequently lost bottom lock, we interpolated depths along the modeled profiles from the high-resolution bathymetry of Figure 3. We used the GRAVMAG program (Pedley, 1991) for modeling. This allows so-called "2.5-D" modeling, in which models are represented by a series of prisms whose axes extend horizontally normal to the plane of the profile. Instead of having infinite length as in 2-D modeling, the prism lengths may be variably set by the user—this is called the "half-strike" length. There is also a facility for limited optimization of the model. Prior to modeling, data were "decimated" to one sample every 100 m. During modeling we created block boundaries as necessary to best fit the positions of the observed magnetic peaks and troughs, and then varied the magnetizations to match the observed amplitudes. GRAVMAG does not provide a "goodness of fit" measure, but in practice we judge a "good fit" to mean a misfit of <200 nT or ~7% of the maximum profile anomaly. The models are shown in Figures 6 and 7.

4. Results

4.1. Sea Surface Magnetics

Figure 2 presents the total magnetic field anomaly at the sea surface and shows a strong E-W lineation. This has not been previously reported in this region, although the anomaly peaks and troughs do correspond to those mapped by Smith et al. (2008). The result of inverting the sea surface field to crustal magnetization is shown in Figure 5. The strong E-W lineation has mostly disappeared, so is attributed largely to artifacts introduced by the 3-D topography.

Previous studies here (Mallows & Searle, 2012; Smith et al., 2008) found anomaly 2 (C2n, 1.77–1.95 Ma, glimpsed at the east and west edges of Figure 5) to be fairly continuous. Measured along E-W lines

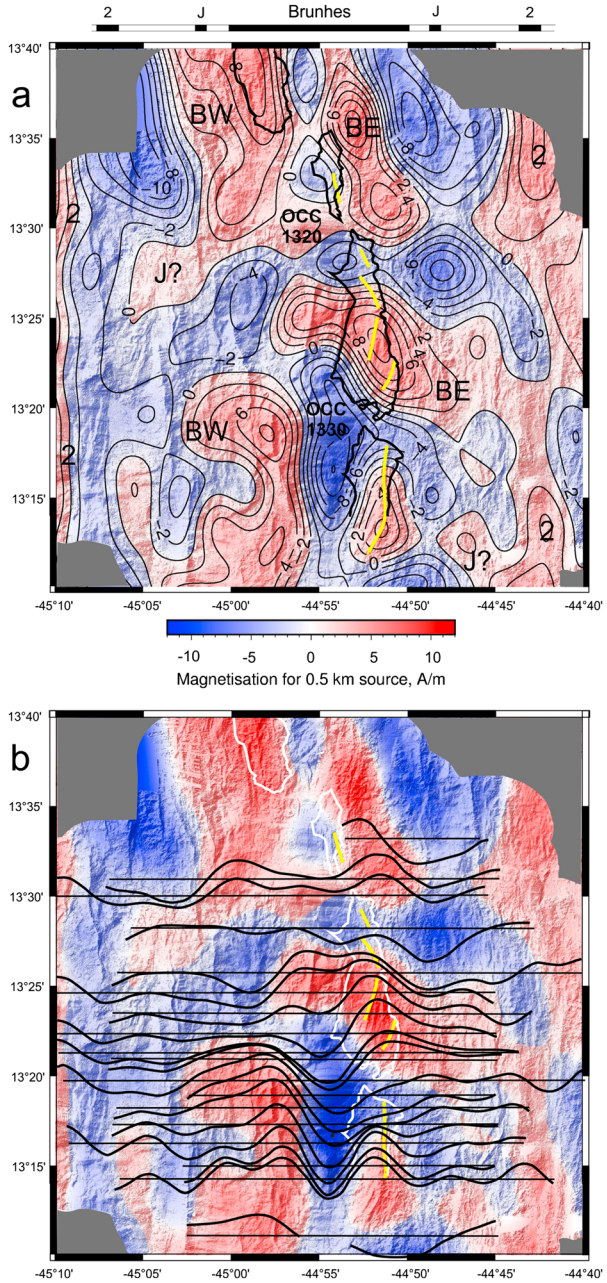

Figure 5. (a) Crustal magnetization inferred from 3-D inversion (Parker & Huestis, 1974) of the magnetic anomalies from Figure 2, assuming a constant 0.5-km-thick source layer, magnetization in the direction of a geocentric axial dipole, and addition of no annihilator (color, with contours every 2 A/m), superimposed on the shaded bathymetry from Figure 1 illuminated from the NW). Thick black line outlines the neovolcanic zone from Mallows and Searle (2012), and yellow marks our best estimate of the current magmatic axis. Predicted reversal history (Cande & Kent, 1985) for the regional 12.5 km/Ma half-spreading rate is shown for comparison at top of the figure. J = Jaramillo. Large characters indicate features interpreted in the text: 2, young edge of normal chron 2; BW, west edge of Brunhes; BE, east edge of Brunhes. (b) The same magnetization image superimposed on shaded relief bathymetry, with superimposed magnetization profiles (heavy black lines) interpolated from the magnetization grid along the E-W tracks shown (fine black lines). White line outlines the neovolcanic zone, and yellow our best estimate of the magmatic axis.

between 13°15′N and 13°33′N, we find the younger sides of anomaly 2 to be separated by 46 ± 3 km (average and standard deviation), close to the 42 km expected based on the regional spreading rate. Our best estimate of the position of the current magmatic axis, based on a combination of topography and acoustic backscatter data, (Figure 5) is several kilometers east of the mid-point between anomalies 2, implying that post-anomaly-2 crustal accretion has been significantly asymmetric. The average asymmetry, expressed as (western half-rate minus eastern half-rate) ÷ (full rate), is 32 ± 6%. Asymmetry is highest (42 ± 1%) south of 13° 19′N; it is 30 ± 3% at the latitudes of the OCC1320 and OCC1330 domes, and lowest (28 ± 2%) between these OCCs.

Younger anomalies are poorly developed. Although there are patches of positive magnetization that might reflect the Jaramillo anomaly (C1r.1n, 0.99–1.07 Ma), for example, near 13°28′N, 45°05′W or at 13°12′N, 44°45′W, that anomaly is generally discontinuous and challenging to trace with confidence. The Brunhes anomaly (C1n, 0–0.78 Ma) is strongly broken up and often displays a negative magnetization near its center. This is particularly striking over the dome of OCC1320, where the strongest negative magnetization occurs (Figure 5). This negative characteristic cannot be removed by adding realistic amounts of annihilator. A similar, although much less well resolved, negative anomaly was observed in the previous studies of Smith et al. (2008) and Mallows and Searle (2012). The total E-W width of the positive magnetization components within this central group ranges from 2 km at 13°27.5′N to 30 km at 13° 30′N, with an average of 12 ± 6 km. This represents only 64% of the expected 19.5-km anomaly width. We note that a discontinuous band of positive magnetization lies along approximately 44°52′W, roughly coincident with the neovolcanic zone mapped by Mallows and Searle (2012). This band is broken by small areas of negative magnetization immediately to the east or SE of OCC1320 and OCC1330, consistent with reduced Brunhes magmatism in these areas as suggested by MacLeod et al. (2009). Only a very narrow band of positive magnetization exists east of the interpreted neovolcanic zone.

4.2. Near-Seabed Microbathymetry

The combined microbathymetry data sets from Figure 3 are interpreted in Figure 8. We adopt the terminology of Escartin et al. (2017) and mostly support their interpretations, except for minor modifications to and extensions of their terrain boundaries.

We are able to map, in detail, areas of unfaulted and faulted hummocky volcanic terrain in the MAR median valley to the north and east of the corrugated dome, or detachment surface, of OCC1320 (Figure 8). Examples can be seen near the center of the axial valley (Figure 9a) and at the eastern edge of Figure 9b where the hanging wall is beginning to be uplifted by the emerging footwall of the detachment to form the OCC "apron." This is the typical hummocky volcanic terrain common to the axial valleys of slow-spreading mid-ocean ridges (Smith & Cann, 1990; Yeo et al., 2012) and is readily recognized in the microbathymetry. The volcanic hummocks are cut in places by faults that occur in clusters with typical widths of 1–2 km, but sometimes as narrow as 500 m or wide as 3 km (Figure 9a). The fault trends typically lie between N-S and ENE-WSW, and rarely ESE-WNW. As noted earlier (Escartin et al., 2017; MacLeod et al., 2009; Mallows & Searle, 2012), these faults thus tend to turn from ridge-axis-

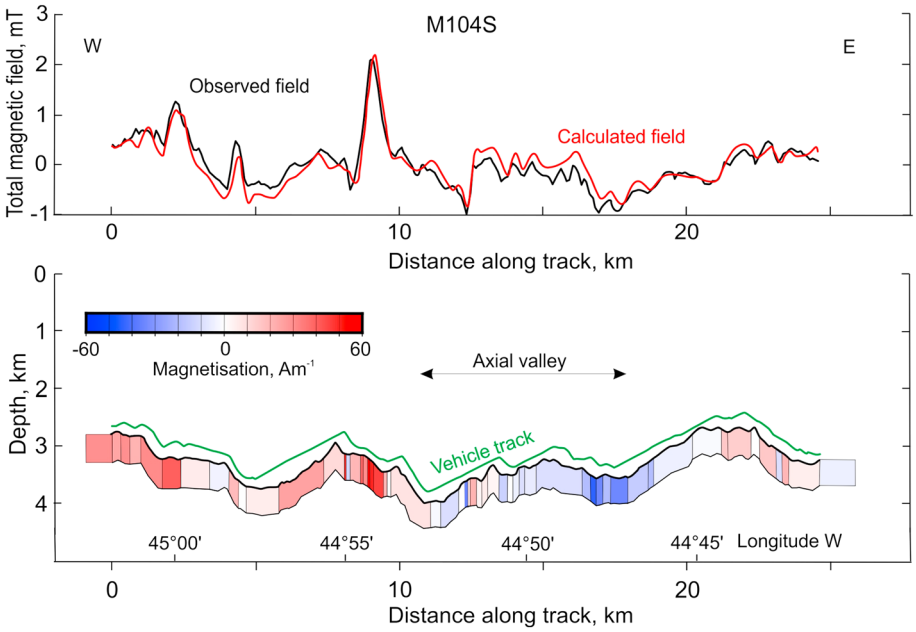

Figure 6. Total magnetic field anomaly from Autosub profile M104S, located midway between oceanic core complexes, and its best fitting 2.5-D model with vertical exaggeration of ~2:1. Source layer is approximately 500 m thick, and magnetized blocks extend 10 km on either side of the plane of the figure. Modeled magnetization ranges from −45 to +60 A/m. Declination of remanent magnetization is 0° and inclination is 25.6° (geocentric axial dipole). Susceptibility is assumed to be zero (see text). Profile location is shown in Figure 1.

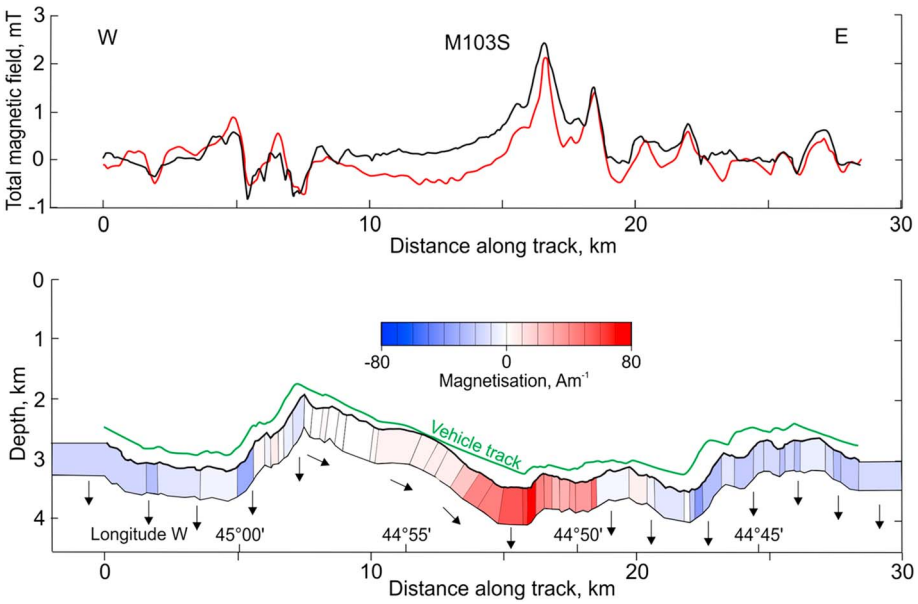

Figure 7. Total magnetic field anomaly from Autosub profile M103S, running along 13°19′N latitude, through the midpoint of OCC1320, and 2.5-D model with vertical exaggeration of ~2:1. Source layer is approximately 500 m thick, and magnetized blocks extend 7.5 km on either side of the plane of the figure. Modeled magnetization ranges from −25 to +71 A/m. Declination of remanent magnetization is 0° and inclination is 25.6° (geocentric axial dipole), except between 14 and 8 km along profile, where they are modified to reflect a gradual rotation of the seafloor following exhumation from 45° (at 14 km) to 65° (at 11 km) anticlockwise about a north horizontal axis, with constant 65° rotation from 11 to 8 km ("chaotic zone"). Small arrows indicate dip direction of remanence in E-W vertical plane. Magnetic boundaries under OCC are rotated from assumed palaeohorizontal. Susceptibility is assumed to be 0.04 SI except over the rotated section (OCC) where it varies between 0.0 and 0.32 SI. Profile location is shown in Figure 1. See text for further explanation.

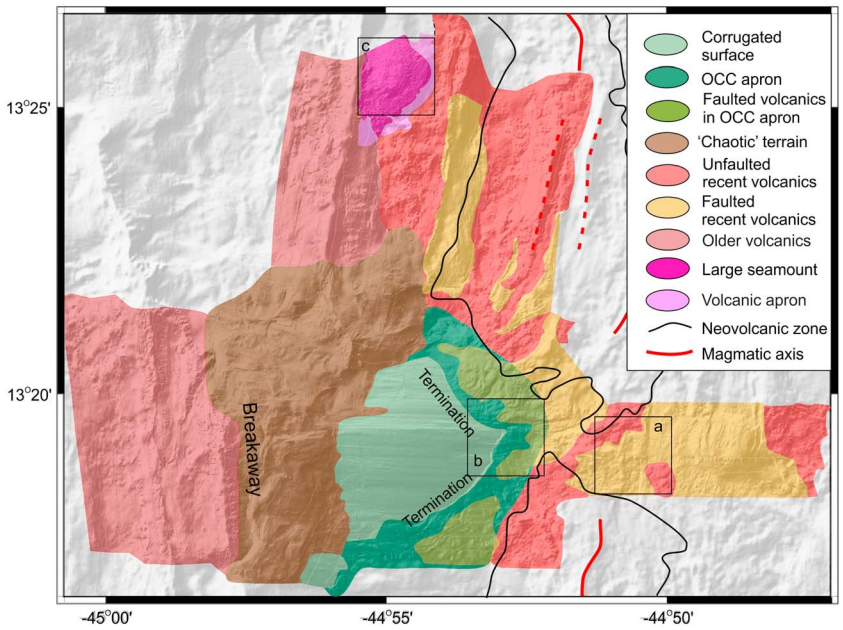

Figure 8. Interpretation of the microbathymetry data from Abyss and Autosub, including and extending the interpretations of Escartin et al. (2017). Data coverage is shown in the inset to Figure 3. Classification colors have been superimposed on shaded relief microbathymetry, illuminated from the NW. Black squares indicate examples shown in Figure 9. OCC = oceanic core complex.

parallel to hanging wall-cutoff-normal, suggesting the cutoff is a low-stress boundary. Different fault trends sometimes crosscut one another, although no consistent overlapping relations can be discerned. The fault scarps range in height from <10 to >100 m. There is no clear line from which the fault sizes consistently increase, or toward which faults dip, that might define a (tectonic) spreading axis. Areas of unfaulted recent volcanics are sparse directly opposite OCC1320 (Figure 8).

We confirm the presence of a narrow apron of lightly deformed seafloor around the base of the OCC dome and marking the hanging wall cutoff (dark green in Figure 8). The apron can be distinguished from the smooth OCC dome and the "normal" median valley floor by changes of slope at its inner and outer edges (Figure 3). That part of the apron proximal to the smooth dome often comprises loose rubble and blocks with pervasive sediment cover (Escartin et al., 2017), but we find its more distal parts have a similar texture to the neighboring "faulted recent volcanics," and such areas are colored lime green in Figure 8.

With our extended coverage, we are also able to trace the "chaotic terrain" of Escartin et al. (2017) farther to the north and south (Figure 8). Our coverage extends some 5 km west of the "breakaway" ridge at 44°57.5′W, where we see tilted fault blocks. These blocks are tilted ~20° away from the MAR axis (Figure 8; Escartin et al., 2017).

Escartin et al. (2017) describe a large, 2-km-wide seamount that occupies the axial valley wall north of OCC1320 (Figure 8, box c). They made an ROV traverse across it, but had no high-resolution bathymetry. Our Autosub microbathymetry (Figure 9c) confirms that the summit is horizontal, not back tilted, and sits on a fault block that has been back tilted ~20°. The summit is covered in individual volcanic hummocks up to ~200 m in diameter, and its flanks are covered with hundreds of small volcanic cones ranging from <25 to ~100 m in diameter and up to ~20 m high. The eastern flank of the seamount has at its base a small east facing scarp ~20 m high, beyond which is a smooth fan of apparently mass-wasted material whose surface dips outward from the volcano at ~30° (Figure 9c). While we cannot measure the age of the volcanism directly, we have seen no other feature showing such a fine volcanic texture in the microbathymetry; this and the untilted summit provide strong hints of a relatively recent origin. Moreover, the strong normal magnetization associated with the seamount (Figures 5 and 6) indicates a Brunhes age. This supports the same conclusion drawn from the fresh appearance and light sediment cover on pillows observed during the ODEMAR ROV dive (Escartin et al., 2017).

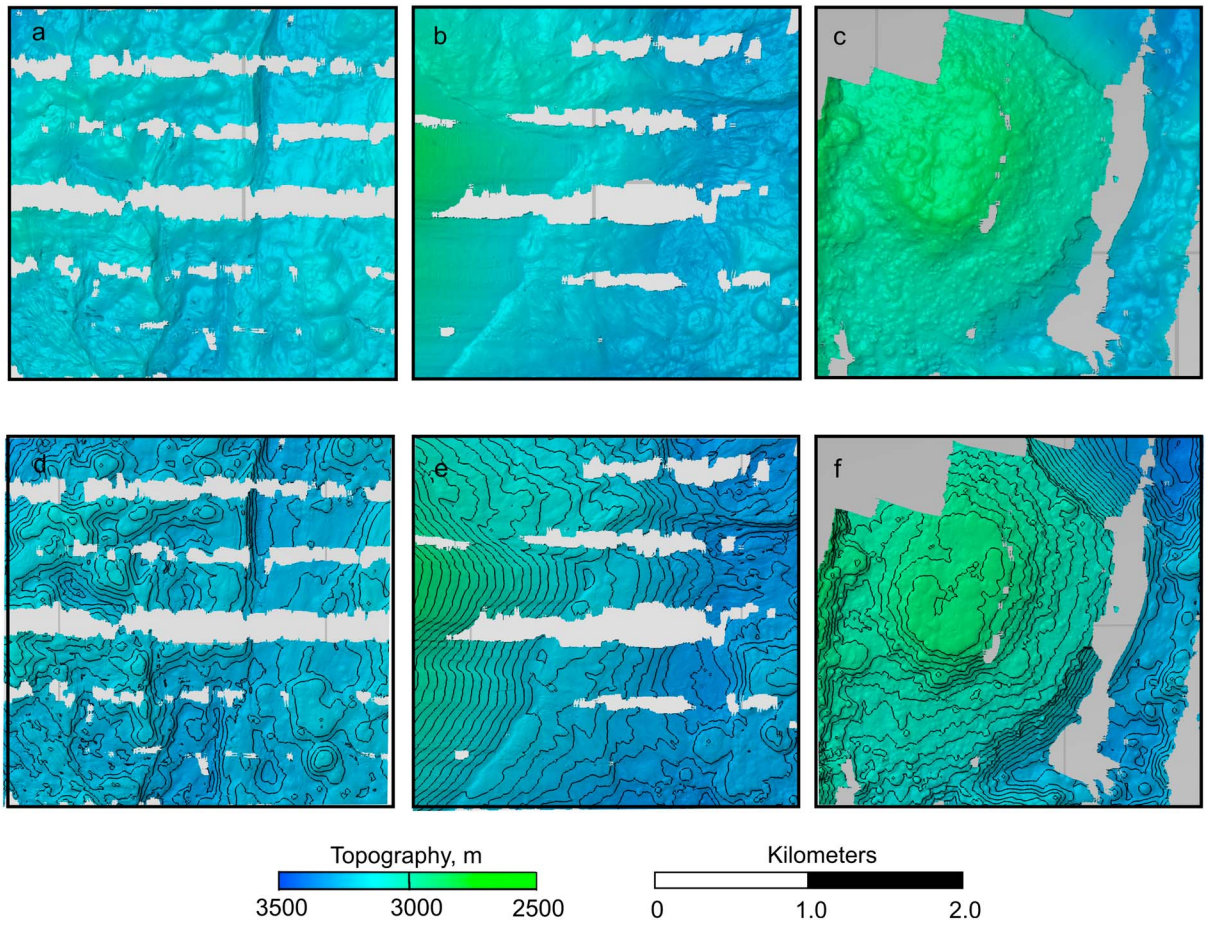

Figure 9. Examples of the autosub microbathymetry, illuminated from the NW with additional ambient lighting (a–c) and with 20-m contours superimposed (d–f). (a, d) Faulted and unfaulted volcanic terrain from the median valley floor east of OCC1320. (b, e) Footwall cutoff (termination) and OCC apron, with toe of corrugated dome and bounding moat on the left. Note that the apron comprises uplifted samples of both hummocky volcanic and obliquely faulted terrain. (c, f) The large off-axis seamount showing its flat summit top left, with the surrounding flanks and seafloor covered with small volcanic cones. Note the smooth, mass-wasted volcanic apron to the east of the seamount, and recent hummocky volcanoes to the east and west.

4.3. Near-Seabed Magnetics

4.3.1. Overview

Figure 4 presents the total magnetic field anomaly measured by Autosub, following corrections for heading, pitch, jumps in signal level, and removal of the mean value for each dive. Immediately obvious is that the smooth dome of OCC1320 is characterized by fairly uniform, low-amplitude anomalies of <100-nT amplitude. In contrast, the surrounding areas to the north and south, and the axial valley to the east, display anomalies up to ~3,000 nT, while the older seafloor west of the OCC has slightly smaller anomalies of <~1,000 nT. There is a region of positive anomalies just north of the OCC, around 13°22′N, 44°54′W, and another of negative anomalies south of the OCC, around 13°17′N, 44°53′W. At such low magnetic latitudes as this, significant anomalies are produced by the northern and southern edges of magnetized bodies. This pattern hints at what would be produced by a uniformly negatively magnetized body under the smooth corrugated dome, in qualitative agreement with the apparent negative magnetization implied by inversion of the sea surface field (Figure 5). In contrast, west of the smooth dome, between 44°55′W and 45°00′W there are primarily negative anomalies in the north and positive in the south, suggesting a broad region of positive magnetization, again as implied by the sea surface field inversion. However, it is important to remember that the Autosub magnetometer responds mostly to features within a few hundred meters of the instrument, while the sea surface field integrates the effects over several kilometers horizontally and to greater depths. We modeled two of the long E-W profiles run by Autosub, as discussed below.

4.3.2. Profile M104S

M104S runs along latitude 13°25′N and is halfway between OCC1320 and OCC1330. We used a half-strike length of 10 km, placed the top of the magnetic source at the seabed and made the source layer approximately 500 m thick (Figure 6). The models are not very sensitive to the precise shape of the base of the source, and we could equally obtain a reasonable fit using a layer twice as thick with approximately half the intensity of magnetization. The model shown in Figure 6 assumes that magnetization is parallel or antiparallel to a geocentric axial dipole, that is, inclination of 25.6° and declination 0°. With magnetizations parallel to the long-term field direction, susceptibility merely alters the net magnetization strength (by a few percent for realistic susceptibilities and magnetizations of young basalts), not its direction, so we set susceptibility to zero. This should be appropriate for a mostly basaltic source, expected on this line, where the Koenigsberger ratio, Q (ratio of remanent to induced magnetization), is typically $\gg 1$. However, if there were significant amounts of gabbro or altered peridotite, we might have $Q \sim 1$, in which case the higher susceptibility would tend to enhance apparent normal polarity and decrease apparent reversed polarity (Tivey & Tucholke, 1998).

Profile M104S can be well matched by a selection of normally and reversely magnetized blocks (Figure 6). Modeled magnetizations range from +60 A/m (at 9 km along the profile, coincident with the off-axis seamount), to −45 A/m (at 17 km), but are otherwise mostly less than the 42 A/m measured on samples of "zero-age" lavas from elsewhere (e.g., Johnson & Tivey, 1995). Mostly, the model shows coherent regions of normally magnetized (at 0–11 and 22–25 km) and reversely magnetized seafloor, although with variations in magnetization intensity and occasionally of polarity direction (e.g., at 3–4 and 23 km). There is a transition from generally normal magnetization west of about 11 km to negative (reverse) magnetizations east of there, which may mark the eastern boundary of the Brunhes anomaly (chron C1n, 0–0.78 Ma). The normally magnetized zone between 22 and 25 km might mark the Jaramillo positive chron (C1r.1n, 0.99–1.07 Ma), although it is rather wider than the predicted 1 km and considerably farther than the predicted 3.6 km from the presumed Brunhes/Matuyama boundary. No obvious western Brunhes boundary or western Jaramillo anomaly are seen. In fact, the model shows mostly normal magnetization west of 44°57.5′W, which is the western edge of the axial positive magnetization seen in the sea surface-inferred magnetization at this latitude. We see this difference as an example of the heterogeneous, 3-D nature of the magnetization distribution here, coupled with the very different volumes that are sensed by the sea surface and near-bottom magnetometers.

4.3.3. Profile M103S

In view of the shape of the OCC topography, we used a half-strike of 7.5 km as being more appropriate for profile M103S (Figure 7). For this profile it was harder to achieve a good fit. In particular, a long-wavelength misfit of some 500 nT remains under the central part of the profile. Nevertheless, we obtained reasonable matches to the various magnetic anomaly peaks and troughs.

Although a reasonable fit to the anomaly as a whole could be obtained assuming a geocentric axial dipole as for M104S, it is likely that the crust (and magnetization vector) under the OCC have been rotated (Mallows & Searle, 2012; Parnell-Turner et al., 2016; Smith et al., 2008). MacLeod et al. (2011) showed that the magnetic vector of the footwall at the 15°45′N OCC on the MAR had undergone a total rotation ~65° (where a negative rotation indicates an anticlockwise rotation) about a north pointing axis. Some of this rotation may have occurred sub-seafloor prior to emergence (e.g., MacLeod et al., 2009). In Figure 7 we assumed that the crust and its natural remanent magnetization (NRM) emerged at the termination or hanging wall cutoff (14 km along profile) already rotated −45°, and then progressively rotated a further −20° between 14 and 11 km along profile (the western edge of the smooth dome) and remained at the final value of −65° from 11 to 8 km (throughout the "chaotic terrain"). This means the magnetization vector rotates from declination +18.6°, inclination +18.6° near the hanging wall cutoff to declination +23.3°, inclination +11.4° at the east edge of the chaotic terrain. However, other rotations (e.g., up to max −45°) can be accommodated by modifying the modeled magnetizations by mostly <10 A/m.

It is not obvious what the orientation of magnetization boundaries should be under an OCC. In the model of Figure 7 we have assumed that "isochrons" reflected in the OCC NRM were horizontal at depth and rotated during exhumation. Thus, the boundaries between modeled blocks are tilted to represent this. In practice the orientation of these boundaries has little effect on the model fit. We recognize that very near bottom, well-

navigated magnetic field observations might resolve this dip (e.g., Xu & Tivey, 2016), but our data are inadequate for such an exercise.

The model of Figure 7 has variable susceptibility to reflect a probably variable lithology. Basalts generally have low susceptibility, but gabbros and serpentinized peridotite, which probably occur in the detachment footwall, may have higher values. Outside the OCC, where we expect the magnetic source to be mostly basaltic, we use a susceptibility of 0.04 SI (explicitly modeling the induced field, even though in this region we assume an axial geocentric dipole). Under the OCC, we allow the remanent magnetization and the susceptibility to vary and find the best fitting values using GravMag's optimization routine. The resultant NRM under the OCC is low, ranging from 0 to 2 A/m in the chaotic terrain to 7 A/m near the termination. Susceptibility varies throughout the OCC between 0 and 0.32 SI.

Modeled magnetization amplitudes are mostly low (less than +25 A/m), except at the OCC apron and axial valley floor, where they progressively increase from 21 A/m at 13 km to a maximum of 71 A/m at 16 km along profile (Figure 7). The latter is the highest magnetization value along the whole profile and occurs on the west flank of a volcanic ridge in the axial valley. Magnetization under the OCC increases eastward from near zero at the breakaway ridge (8 km) to 7 A/m just west of the hanging wall cutoff (13 km). Positive magnetization is seen around the OCC from 8 to 18 km, and intermittently west of the OCC to 6 km. If some or all of this were Brunhes age crust, the Brunhes width here would be between 10 and ~14 km, some 5 km less than predicted but comparable to the values inferred from the sea surface field (see discussion below).

East of the detachment, the seafloor becomes (and remains) reversely magnetized from 18 km to the end of the profile. If we were to assume that the plate boundary is at the hanging wall cutoff (13 km) and that the eastern Brunhes-Matuyama boundary is at 18 km, this implies a very low accretion rate of 6.4 km/Ma, just half the predicted rate, in the hanging wall plate, equivalent to an asymmetry of 49%. No evidence of an eastern Jaramillo anomaly is seen on this profile, but a weakly normally magnetized patch near 8 km might mark it in the west.

Once again, this magnetization distribution (positive under the smooth dome) is in contrast to that inferred from the sea surface data, and again, we attribute this mostly to significant 3-D and imaging volume effects. The rotated magnetization under the OCC does not appear to have enough effect to reverse the sign of the anomaly (in 2-D). In view of this mismatch and the extreme variability of the crustal magnetization, coupled with the relatively sparse lateral profile coverage, further speculation on anomaly identifications and spreading asymmetry is not warranted.

5. Discussion

5.1. Comparison of Near-Bottom Magnetic Results With Other Data

Because of the apparent discrepancies between the sea surface and near-bottom magnetic results, we carefully compared our results with earlier studies. A previous deep-towed survey of part of our study area using the TOBI instrument included a 30-kHz side scan sonar survey and deep-towed measurement of the magnetic field (MacLeod et al., 2009; Mallows & Searle, 2012). Figure 10 compares our results from the region of Autosub profile M104S (between OCCs) with the earlier data, and Figure 11 makes the same comparison for profile M103S.

The magnetization profile inferred from TOBI (Figure 10d) has a similar shape to that inferred from the JC132 sea surface data (Figure 10c) although, as expected, with differences in detailed shape and amplitude. These differences result from the higher resolution obtained by TOBI's closer proximity to the seafloor (though upward continued to 1.32 km below sea level prior to inversion). Both the 3-D inversion of the TOBI data (colored, contoured image in Figure 10e) and the JC132 sea surface result reveal very nonlinear patterns of magnetization. The magnetization inferred in our 2.5-D model of the Autosub data (Figure 10e) also has a broadly similar pattern to the TOBI result, with normal magnetization in the west and east, and a normally magnetized peak near the center.

In the JC132 sea surface inversion (Figure 10c) the central band of normal magnetization extends from just west of the off-axis seamount (where we image recent volcanic hummocks in the microbathymetry—Figure 9d) to the small ridge near 44°50′W (Figure 10a). This corresponds to the region of high acoustic

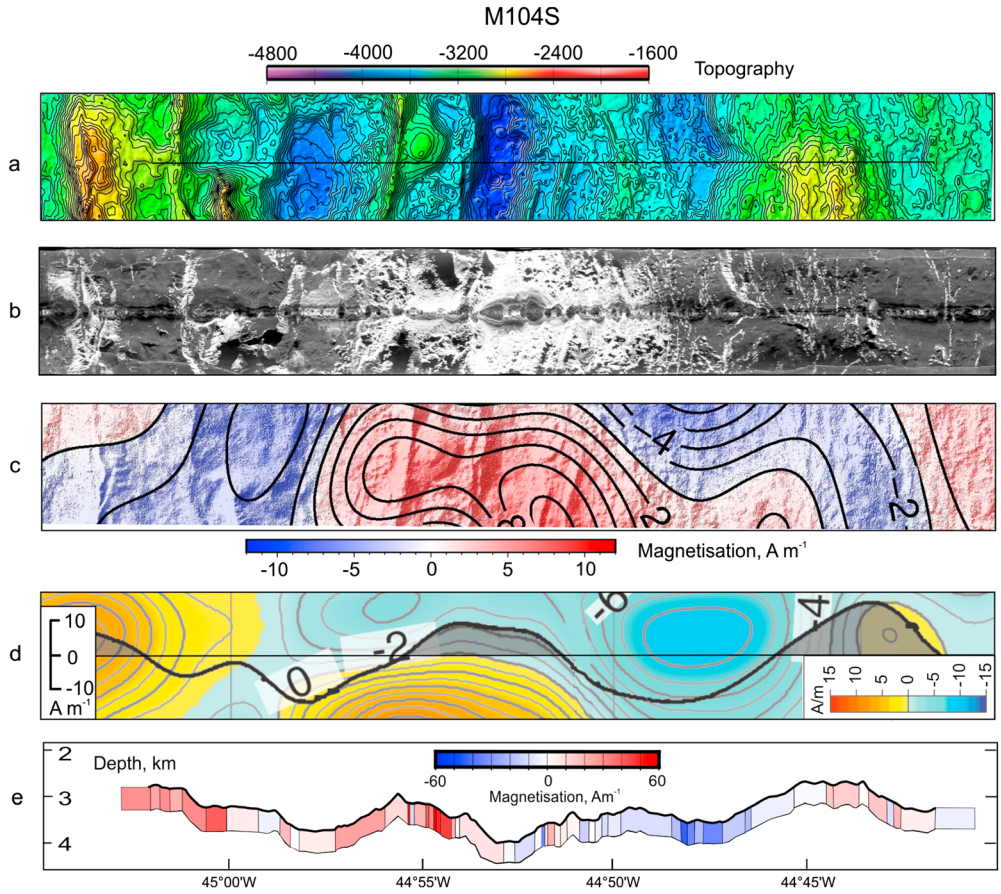

Figure 10. Comparison of our results for profile M104S with previous high-resolution findings. (a) Bathymetry from Figure 1 along a 6-km-wide swathe centered on profile M104S, whose track is marked by the black line. Contours at 20-m intervals. (b) TOBI side scan sonar mosaic covering the same swathe as (a), from Mallows and Searle (2012). Track line is along center of swathe, so insonification is northward in the top and southward in the bottom of the figure. High backscatter is white. (c) Magnetization from 3-D inversion of JC132 sea surface magnetic field, taken from Figure 5 over same area as (a). Contours at 2-A/m intervals. (d) Magnetization over same area as (a) from Mallows and Searle (2012). Colored image contoured at 1 A/m shows result of 3-D inversion of the TOBI field after upward continuation to 1.32 km below sea level, with scale bar at bottom right. Profile with positive areas shaded shows result of 2-D inversion of upward continued field along the TOBI track line, with scale bar at left. Fine gray lines show latitude and longitude at 10′. intervals. (e) Magnetization model for Autosub profile M104S from Figure 6. Longitude scale in (e) applies to all panels.

backscatter on the side scan image (Figure 10b), although the seamount, lying directly under the TOBI track, was poorly imaged and was attributed a slightly greater age by Mallows and Searle (2012) on the basis of backscatter level alone. High magnetization is associated with the seamount in the JC132 sea surface inversion (Figure 10c), the TOBI 2-D profile (Figure 10d), and the Autosub magnetic model (Figure 10e). Enhanced positive magnetization often marks the youngest seafloor basalts (e.g., Allerton et al., 2000; Hussenoeder et al., 1996; Tivey & Johnson, 1987), so we take this as good evidence that the seamount is relatively young, as inferred by Escartin et al. (2017) on the basis of video evidence. It is thus effectively part of the neovolcanic zone and shows that magmatism at this detachment-rich spreading center is not fully focused along an axial line. Similar off-axis volcanism has been recorded in the Mid-Cayman Spreading Center (Searle, 2012).

East of the seamount, a combined interpretation of the side scan and the topography suggests that high backscatter (young) lavas probably erupted from the ridge at 44°51′W and flowed west, to pond in the valley at 44°53′W (Mallows & Searle, 2012). The inverted sea surface magnetization shows the presence of normally magnetized material here. The Autosub magnetic model has a small amount of reversed magnetization in this region, as does the TOBI 3-D inversion, although the signal is quite three-dimensional. It could be

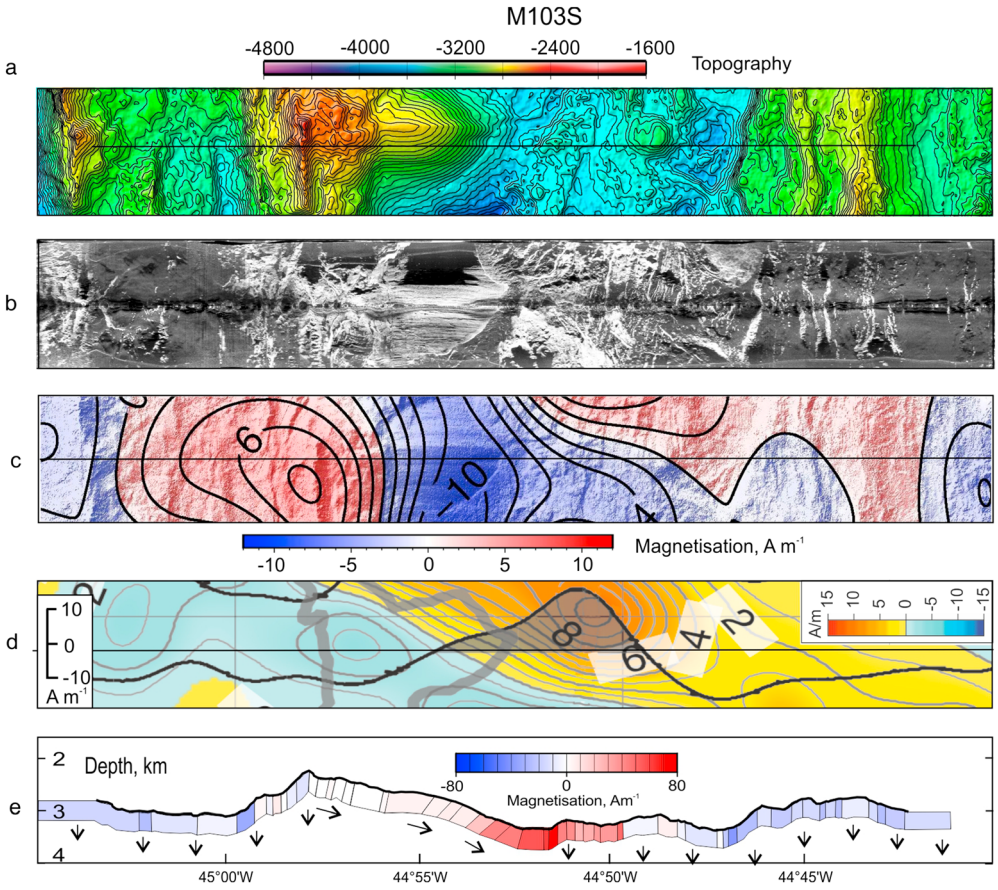

Figure 11. Comparison of our results for profile M103S with previous high-resolution findings. (a) Bathymetry from Figure 1 along a 6-km-wide swathe centered on profile M103S, whose track is marked by the black line. Contours at 20-m interval. (b) TOBI side scan sonar mosaic covering the same swathe as (a), after Mallows and Searle (2012). Track line is along center of swathe, so insonification is northward in the top and southward in the bottom of figure. High backscatter is white. (c) Magnetization from 3-D inversion of JC132 sea surface magnetic field, taken from Figure 5 over same area as (a). Contours at 2 A/m. (d) Magnetization over same area as (a) after Mallows and Searle (2012). Colored image contoured at 1 A/m shows result of 3-D inversion of the TOBI field after upward continuation to 1.32 km below sea level, with scale bar at bottom right. Profile with positive areas shaded shows result of 2-D inversion of upward continued field along the TOBI track line, with scale bar at left. Fine gray lines show latitude and longitude at 10′ intervals. Thick gray line marks the approximate outline of OCC1320. (e) Magnetization model for Autosub profile M103S from Figure 7. Longitude scale in (e) applies to all panels.

that a thin veneer of recent lavas overlies a more substantial pile of older, reversely magnetized ones, with the Autosub and TOBI magnetometers being more sensitive to this veneer. It may also be that the high apparent magnetization associated with the seamount reflects a thicker than usual magnetic source associated with the volcano.

Figure 11 shows a similar comparison for profile M103S across OCC1320. Here there is a stronger contrast between the inversion of the JC132 sea surface field and the TOBI results. In particular, the strong negative magnetization associated with OCC1320 in the inverted sea surface field (Figure 11c), although visible in the TOBI result, is displaced westward (Figure 11d). The positive magnetization seen between 44°56′W and 45°03′W in the inverted sea surface field is completely absent from both the 2-D and 3-D TOBI inversions. The magnetization east of 44°50′W is strongly negative in the TOBI 2-D inversion, positive in the TOBI 3-D result, but varies around zero in the sea surface field inversion. The shape of the magnetization inferred in the 2-D TOBI inversion is similar to that inferred from Autosub (Figure 11e) with a central positive flanked by negative troughs, although the detailed positions of the peaks, troughs, and polarity bounds are slightly different. Nevertheless, the magnetization low

centered at 44°54′W in the sea surface inversion and at 44°56′W in both TOBI inversions is either absent or displaced to approximately 45°00′W in the Autosub model. We note again the very significant departure of the TOBI 3-D inversion from N-S linearity.

The TOBI (Figure 11d) and Autosub (Figure 11e) results show high magnetization around 44°51′W to 44°52′W. The TOBI side scan image (Figure 11b) shows moderate-to-low backscatter in this region, which is inferred to be one where recent volcanism is sparse or absent, reflecting a low magmatic state of the MAR during active detachment faulting (MacLeod et al., 2009). We concur with the latter interpretation and suspect that the relatively high magnetization levels seen here by TOBI and Autosub at least partly reflect the nearby presence of the neovolcanic zone to the south (Figure 5), the northern tip of which can just be seen at 44°50′W at the bottom of Figure 11b. It is also possible that the area just east of the hanging wall cutoff is a "keystone" block stranded between the OCC detachment and a zone of weak magmatism feeding the footwall (Buck et al., 2005) where lavas have accumulated into a pile significantly thicker than the 0.5 km assumed in our magnetic model, producing a high apparent magnetization even with basalts of moderate age and magnetization.

In both the M104S and M103S areas the shape of the TOBI 2-D inverted magnetization matches the Autosub models fairly closely and gives us confidence that there are no major errors in our data or modeling. Rather, it appears that the magnetization distribution here is strongly three-dimensional. A further possible complication arises from the assumption that, in the sea surface inversion and outside OCC1320, the magnetic boundaries are assumed vertical, whereas in fact they may have significant tilt (see Xu & Tivey, 2016). Further progress in understanding the magnetization here will have to await the acquisition of further high-resolution near-seafloor data to allow full 3-D modeling.

5.2. Sea Surface Magnetic Field and the Seafloor Spreading History

Despite the vagaries of the near-bottom magnetic results, we can use the sea surface data to explore the broad-scale magmatic history of the region. The magnetization pattern shown in Figure 5 is very different to that predicted by a history of uniform spreading at the regional rate. While anomaly 2 appears continuous, and the spacing of this anomaly pair on either side of the axis is close to that expected for the predicted spreading rate, the post-anomaly-2 reversal history is extremely variable and, based on the current location of the magmatic axis, asymmetric. The normally magnetized seafloor in the center of our study area has a very variable width, on average only 64% of that predicted for the Brunhes. It is mostly discontinuous, containing "inliers" of reversely magnetized, presumably older, seafloor, and is virtually absent in places, such as 13°19′N and 13°28′N (Figure 5). This supports, at higher resolution, the pattern previously observed by Smith et al. (2008) and Mallows and Searle (2012).

A similarly disorganized and partly discontinuous Brunhes anomaly is seen on the nearby detachment-rich MAR segment at 14°30′N to 15°40′N (Fujiwara et al., 2003), while a narrowed Brunhes (10-km width) occurs at the 16°30′N segment, also characterized by detachment faulting (Parnell-Turner et al., 2016). Both Fujiwara et al. (2003) and Parnell-Turner et al. (2016) suggest that variable lithology (e.g., the presence of abundant peridotite rather than extensive basalt) could account for low amplitude Brunhes anomalies. However, this alone cannot explain the occurrence of reversed magnetization within the Brunhes nor of a narrower than expected region of normal magnetization.

In our region, a band of positive magnetization extends discontinuously N-S along approximately 44°52′E. Comparison with the neovolcanic zone inferred from TOBI side scan sonar reveals that the NVZ is generally closely associated with these regions of positive magnetization, and the gaps within the NVZ correspond approximately to gaps in the normal magnetization (Figure 5). While the correspondence is not perfect, it strongly suggests to us that Brunhes age (0–0.78 Ma) magmatism was subdued opposite the 13°20′N and 13°30′N OCCs but was (and is) abundant between them, as predicted by the model of MacLeod et al. (2009). However, this band of normal magnetization is at most only about 8-km wide, which would correspond to less than half the expected width of the Brunhes. There is a further, slightly wider band of normally magnetized crust (also discontinuous) to the west, around 44°59′W, but it is not wide enough to make up the full expected Brunhes width. A discontinuous band of negatively (reversely) magnetized crust lies between the two positive bands, approximately along 44°55′W.

There are two possible mechanisms to explain the presence of young, near-axis reversed magnetization. First, deep-seated peridotite could have been reversely magnetized during the Matuyama period via deeply penetrating fluids beneath a thinned crust (MacLeod et al., 2009, 2011). This might then have been exhumed when active normal faulting of Matuyama age continued into the Brunhes to form a detachment fault, so the reversely magnetized material could now be in place under the OCC1320 dome as suggested by Figure 5. We note that in this case the N-S elongation of the reversely magnetized body beyond the OCC1320 dome implies ridge-ward prolongation of the detachment. The Curie isotherm under mid-ocean ridge axes could be as deep as 8 km (Salem et al., 2014) or more, so such a deep-seated origin of the magnetization is feasible. This explanation for OCC1320 would require some 10 km of exhumation at the half-spreading rate. The same explanation is harder to apply to OCC1330, whose center is characterized by normally magnetized material (although with reversed material on its north and south flanks). However, this OCC has a different spreading history to OCC1320 and has been defunct for some time (Escartin et al., 2017; MacLeod et al., 2009).

Second, there could be significant jumping or migration of the magmatic "axis," and the observed asymmetry supports this. Buck et al. (2005) and MacLeod et al. (2009) showed that detachment faulting can lead to significant cross-axis migration of the active plate boundary. The presence of detachment faults also provides a strong control on the location and quantity of melt delivery to the crust (MacLeod et al., 2009). In particular, melt delivery to the hanging walls of detachments should be greatly diminished, and the distribution of presumed Brunhes age crust seen in Figure 5 confirms this. Moreover, the neovolcanic zone as inferred from high side scan sonar backscatter is interrupted in these same areas (and the seafloor there is extensively faulted; Figure 8) but elsewhere correlates moderately well with areas of positive magnetization. Our estimates of the asymmetry of crustal accretion show significant asymmetry of 30–40% throughout the segment, although it is slightly lower (28%) between the two OCCs than at their latitudes (30%).

In addition to the occurrence of reversely magnetized material "within" the Brunhes, the narrower than expected (or even absence of) Brunhes age crust implies either a significant slowing of the spreading rate, which is not seen at nearby "magmatic" spreading regions such as the 14°N segment of the MAR (Fujiwara et al., 2003), or a concentration of lava into a narrower but thicker body than usual. This latter could occur via successive emplacements of magma or lava being added in a vertical pile, with younger material emplaced on (or within) existing deposits. Such a process may well occur in the valleys of the axial zone, just east and north of OCC1320 where, as discussed above, some lavas may flow from "axial volcanic ridges" and pond in the adjacent valleys to their west. Also, the western edge of the OCC1320 hanging wall may have become trapped between the detachment fault and a weak magmatic intrusion zone to the east (Buck et al., 2005), thus accumulating a stack of lavas over a considerable time in a horizontally reduced space (Allerton et al., 2000; Parnell-Turner et al., 2016).

Wider than predicted polarity bands could be produced when predominantly magmatic spreading diminishes and is replaced by extensive tectonic extension (including of course detachment formation and slippage), which would "spread" and thin previously formed crust without the injection of new magma. An example of this is seen immediately east of OCC1320, where extensive faulting seen in the Autosub microbathymetry and TOBI side scan sonar disrupts the previous pattern of hummocky volcanism (Figure 9a). The combination of variable and migrating melt emplacement zones, jumping of plate boundaries from axial volcanic ridges to axial valley bounding (and subsequently detachment) faults together with focusing of lava into localized deeps, coupled with periods of nonmagmatic tectonic extension could lead to a very complex crustal magnetization pattern in 3-D (e.g., Schouten et al., 1982).

While all the details of the tectonic development of this segment are still unclear, we can suggest the following broad general history for this region. Relatively uniform but slightly oblique spreading with minor extension on valley-wall faults was occurring around anomaly 2 time (~1.8 Ma) and probably continued early into the Brunhes (<0.78 Ma before present), as indicated by the fairly continuous positive/negative/positive succession from the west edge of Figure 5 to about 44°58′W ("2" to "BW" on Figure 5a). At this point, with diminishing axial magmatism, detachment faulting and asymmetric spreading were initiated. The main plate boundary jumped westward (from near "BE" in southern half of Figure 5a) to the detachments (near the eastern ends of OCC1320 and OCC1330), major magmatic emplacement opposite the detachments ceased, previously emplaced magmatic crust was tectonically extended, and deep-seated previously

reversely magnetized material was exhumed under OCC1320, and perhaps to a lesser extent on the north and south flanks of OCC1330. The absence of negative magnetization at the core of OCC1330 might reflect the presence of a different lithology, such as a higher proportion of high-susceptibility material, or the effect of younger gabbro intrusions. This change accompanied a transition to completely orthogonal spreading with widespread OCC formation and resulted in highly asymmetric crustal accretion and the creation of a nontransform discontinuity around13°37′N (Figure 1). A variable and migrating melt supply controlled by the detachment faulting, together with extensive tectonic extension throughout the remainder of the Brunhes has led to the complex pattern observed today (Figure 5). Finally, if our explanations for the highly discontinuous magmatic pattern implied by the crustal magnetization are correct, they argue against the model of single, segment-long connected detachment faults and in favor of independent evolution of OCCs and detachments.

5.3. Autosub Performance

This was the first time Autosub was used extensively for a mid-ocean ridge study. The main problem encountered was the loss of bottom lock by the Doppler acoustic profiler on which the AUV navigation relied. This occurred when the vehicle was unable to follow parts of the steep terrain encountered around the ridge axis. In an attempt to ameliorate this, we planned tracks to be as close as possible to contour following around OCC1320, but this was impossible for the long traverses. Clearly, other strategies will need to be followed in future campaigns, including probably flying lower and slower. Another problem (for the magnetometer) was the severe pitch excursions experienced (up to 18°), which were unanticipated. When future "figure-of-eight" turns are carried out to calibrate the magnetometer for vehicle motion, it will be important to program such pitch variations into the turns.

We obtained good microbathymetry data and were able to combine them with other data (Figure 3). However, careful analysis showed that there were significant offsets (up to ~50 m) between the data sets and possibly even between different Autosub dives. Careful attention will need to be paid to improving the navigation and calibrating the depth measurements in future.

6. Conclusions

We have collected closely spaced sea surface magnetic field data during the acquisition of a grid of seismic profiles, and near-seabed magnetic field and microbathymetry data during AUV dives made in between seismic profiling. These magnetic data show a disorganized pattern of crustal magnetization throughout the 13°N area. Anomaly 2 is well imaged and spaced as expected for the regional spreading rate, but younger anomalies are not. The onset of extensive detachment faulting and OCC formation, beginning sometime after chron C2n (~1.8 Ma), is marked by a major disruption of the magmatic pattern. Subsequently, both magmatic and tectonic extension have been laterally and temporally variable and have apparently not followed a long-term coherent spreading axis. Unequivocal Jaramillo anomalies are not observed in either the sea surface or near-seabed data. The Brunhes anomaly is, on average, some 64% of the width expected given the regional spreading rate. It is discontinuous along-axis and frequently divided into several components across axis, separated by areas of negative, presumably reversed, magnetization. Anomalously narrow magnetic source widths could be explained by localized ponding of lavas, and wider than expected polarity bands could be caused by significant postemplacement tectonic stretching including detachment faulting. We suggest that an area of reversely magnetized crust "within" the Brunhes anomaly, associated with OCC1320, could be explained by exhumation of deep, older and reversely magnetized lithosphere along the detachment fault. Other areas of reversed magnetization within the Brunhes may result from extensive episodic migration of the magmatic axis and development of detachments off-axis.

Our microbathymetry data complement and extend those previously available over OCC1320 and support conclusions drawn from previous studies. We mapped numerous small volcanic cones on and around an off-axis seamount at 13° 25′N and infer that volcanism has been recently active there in an example of recent off-axis volcanic emplacement onto older crust.

The near-seabed magnetic data acquired by Autosub suffer from poor vehicle navigation resulting from loss of bottom lock by the on-board Doppler acoustic profiler. Future missions to the MAR will have to take steps to avoid this. Only two profiles had reasonably acceptable navigation allowing magnetic field

modeling. The results of modeling are qualitatively similar to earlier work carried out using the TOBI deep-towed instrument, but there are some apparent inconsistencies with results from the sea surface study. We attribute these to the strongly three-dimensional nature of the topography and magnetization distribution, and to the very different distances of the Autosub and sea surface magnetometers from the magnetic sources. Resolution of the various questions raised by our magnetic survey requires a closely spaced 2-D grid of near-seabed data coupled with fully 3-D interpretation.

Author Contributions

All authors were involved in planning the overall project. Peirce and Reston were co-chief scientists during data acquisition. Searle and MacLeod were principally involved in planning the Autosub mission. Searle oversaw the Autosub mission at sea, carried out most of the data manipulation and modeling, and wrote the paper. All authors contributed to discussion and final editing.

Acknowledgments
This work was funded by the UK Natural Environment Research Council under grants NE/J02029X/1 (Durham: Peirce), NE/J021741/1 (Cardiff: MacLeod), and NE/J022551/1 (Birmingham: Reston). The authors gratefully acknowledge the skill and assistance of the officers, engineers, crew, technicians, and shipboard science party of RRS James Cook cruise JC132. We thank Géraud Vilaseca for the initial processing of the Autosub microbathymetry. We are grateful to Javier Escartin for providing the ODEMAR microbathymetry data prior to its publication and Maurice Tivey for assistance with the magnetic inversion programs and for a very detailed and helpful review. We also thank Roi Granot and Antony Morris for their helpful reviews. Most figures were prepared using the Generic Mapping Tools (Wessel & Smith, 1998). All data from cruise JC132 are archived at the NERC's British Oceanographic Data Center (www.bodc.ac.uk).

References

Allerton, S., Escartin, J., & Searle, R. C. (2000). Extremely asymmetric magmatic accretion of oceanic crust at the ends of slow-spreading ridge-segments. *Geology*, *28*(2), 179–182. https://doi.org/10.1130/0091-7613(2000)28<179:EAMAOO>2.0.CO;2

Buck, W. R., Lavier, L., & Poliakov, A. N. B. (2005). Modes of faulting at mid-ocean ridges. *Nature*, *434*(7034), 719–723. https://doi.org/10.1038/nature03358

Cande, S., & Kent, D. (1995). Revised calibration of the geomagnetic polarity timescale for the late Cretaceous and Cenozoic. *Journal of Geophysical Research*, *100*, 6093–6095. https://doi.org/10.1029/94JB03098

Cann, J. R., Smith, D. K., Escartin, J., & Schouten, H. (2015). Tectonic evolution of 200 km of Mid-Atlantic Ridge over 10 million years, interplay of volcanism and faulting. *Geochemistry, Geophysics, Geosystems*, *16*, 2303–2321. https://doi.org/10.1002/2015gc005797

DeMets, C., Gordon, R. G., & Argus, D. F. (2010). Geologically current plate motions. *Geophysical Journal International*, *181*, 1–80. https://doi.org/10.1111/j.1365-246X.2009.04491.x

Erwan, T., Finlay, C. C., Beggan, C. D., Alken, P., Aubert, J., Barrois, O., Bertrand, F., et al. (2015). International Geomagnetic Reference Field: The 12th generation. *Earth, Planets and Space*, *67*(1). https://doi.org/10.1186/s40623-015-0228-9

Escartin, J., Mevel, C., Petersen, S., Bonnemains, D., Cannat, M., Andreani, M., Augustin, N., et al. (2017). Tectonic structure, evolution, and the nature of oceanic core complexes and their detachment fault zones (13°20′N and 13°30′N, Mid Atlantic Ridge). *Geochemistry, Geophysics, Geosystems*, *18*, 1451–1482. https://doi.org/10.1002/2016gc006775

Escartin, J., Smith, D. K., Cann, J., Schouten, H., Langmuir, C. H., & Escrig, S. (2008). Central role of detachment faults in accretion of slow-spreading oceanic lithosphere. *Nature*, *455*(7214), 790–794. https://doi.org/10.1038/nature07333.

Fujiwara, T., Lin, J., Matsumoto, T., Kelemen, P. B., Tucholke, B. E., & Casey, J. F. (2003). Crustal evolution of the Mid-Atlantic ridge near fifteen-twenty fracture zone in the last 5 Ma. *Geochemistry, Geophysics, Geosystems*, *4*(3), 1024. https://doi.org/10.1029/2002GC000364.

Hussenoeder, S. A., Tivey, M. A., Schouten, H., & Searle, R. C. (1996). Near-bottom magnetic survey of the Mid-Atlantic Ridge axis, 24°-24°40′N, implications for crustal accretion at slow spreading ridges. *Journal of Geophysical Research*, *101*, 22,051–22,069. https://doi.org/10.1029/96JB01890

Johnson, H. P., & Tivey, M. A. (1995). Magnetic-properties of zero-age oceanic-crust—A new submarine lava flow on the Juan-De-Fuca Ridge. *Geophysical Research Letters*, *22*, 175–178. https://doi.org/10.1029/94GL02053

MacLeod, C. J., Carlut, J., Escartin, J., Horen, H., & Morris, A. (2011). Quantitative constraint on footwall rotations at the 15 degrees 45′N oceanic core complex, Mid-Atlantic Ridge, Implications for oceanic detachment fault processes. *Geochemistry, Geophysics, Geosystems*, *12*, Q0AG03. https://doi.org/10.1029/2011gc003503

MacLeod, C. J., Searle, R. C., Murton, B. J., Casey, J. F., Mallows, C., Unsworth, S. C., Achenbach, K. L., et al. (2009). Life cycle and internal structure of oceanic core complexes. *Earth and Planetary Science Letters*, *287*(3–4), 333–344. https://doi.org/10.1016/j.epsl.2009.08.016

Mallows, C., & Searle, R. C. (2012). A geophysical study of oceanic core complexes and surrounding terrain, Mid-Atlantic Ridge at 13°–14°N. *Geochemistry, Geophysics, Geosystems*, *13*, Q0AG08. https://doi.org/10.1029/2012GC004075

McPhail, S. (2009). Autosub6000, a deep diving long range AUV. *Journal of Bionic Engineering*, *6*(1), 55–62. https://doi.org/10.1016/S1672-6529(08)60095-5

Parker, R. L., & Huestis, S. P. (1974). The inversion of magnetic anomalies in the presence of topography. *Journal of Geophysical Research*, *79*, 1587–1593. https://doi.org/10.1029/JB079i011p01587

Parnell-Turner, R., Schouten, H., & Smith, D. K. (2016). Tectonic structure of the Mid-Atlantic Ridge near 16°30′N. *Geochemistry, Geophysics, Geosystems*, *17*, 3993–4010. https://doi.org/10.1002/2016GC006514

Parnell-Turner, R., Sohn, R. A., Peirce, C., Reston, T. J., MacLeod, C. J., Searle, R. C., & Simão, N. M. (2017). Oceanic detachment faults generate compression in extension. *Geology* https://doi.org/10.1130/G39232.1, *45*(10), 923–926.

Pedley, R. C. (1991). GRAVMAG—Interactive 2.5D gravity and magnetic modelling program. Keyworth, Nottingham, U.K., British Geological Survey.

Peirce, C. (2014a). RRS James Cook JC102 cruise report, the role and extent of detachment faulting at slow-spreading mid-ocean ridges, leg 1. Durham University, Department of Earth Sciences, 19 pp.

Peirce, C. (2014b). RRS James Cook JC109 cruise report, the role and extent of detachment faulting at slow-spreading mid-ocean ridges, leg 2. Durham University, Department of Earth Sciences, 26 pp.

Reston, T. & Peirce, C. (2016). RRS James Cook JC132 cruise report, the role and extent of detachment faulting at slow-spreading mid-ocean ridges, leg 3. Birmingham University, School of Geography, Earth and Environmental Sciences, 62 pp.

Reston, T. J., & Ranero, C. R. (2011). The 3-D geometry of detachment faulting at mid-ocean ridges. *Geochemistry, Geophysics, Geosystems*, *12*, Q0AG05. https://doi.org/10.1029/2011GC003666

Salem, A. E., Green, C., Ravat, D., Singh, K., East, P., Fairhead, J. D., & Biegert, E. (2014). Depth to curie temperature across the Central Red Sea from magnetic data using the de-fractal method. *Tectonophysics*, *624-625*, 75–86. https://doi.org/10.1016/j.tecto.2014.04.027

Schouten, H., Denham, C., & Smith, W. (1982). On the quality of marine magnetic anomaly sources and seafloor topography. *Geophysical Journal of the Royal Astronomical Society*, *70*(1), 245–259. https://doi.org/10.1111/j.1365-246X.1982.tb06403.x

Schouten, H., Smith, D. K., Cann, J. R., & Escartín, J. (2010). Tectonic versus magmatic extension in the presence of core complexes at slow-spreading ridges from a visualization of faulted seafloor topography. *Geology*, *38*(7), 615–618. https://doi.org/10.1130/G30803.1

Searle, R. C. (2012). Are axial volcanic ridges where all the (volcanic) action is? Invited paper OS11E-06 presented at American Geophysical Union Fall Meeting, San Francisco.

Smith, D. K., & Cann, J. R. (1990). Hundreds of small volcanoes on the median valley floor of the Mid-Atlantic Ridge at 24–30°N. *Nature*, *348*(6297), 152–155. https://doi.org/10.1038/348152a0

Smith, D. K., Cann, J. R., & Escartin, J. (2006). Widespread active detachment faulting and core complex formation near 13°N on the Mid-Atlantic Ridge. *Nature*, *442*, 440–443. https://doi.org/10.1038/nature04950

Smith, D. K., Escartin, J., Schouten, H., & Cann, J. R. (2008). Fault rotation and core complex formation, significant processes in seafloor formation at slow-spreading midocean ridges (Mid-Atlantic Ridge, 13°–15°N). *Geochemistry, Geophysics, Geosystems*, *9*, Q03003. https://doi.org/10.1029/02007GC001699

Tivey, M. A., & Johnson, H. P. (1987). The central anomaly magnetic high, implications for ocean crust construction and evolution. *Journal of Geophysical Research*, *92*, 12,685–12,694. https://doi.org/10.1029/JB092iB12p12685

Tivey, M. A., & Tucholke, B. E. (1998). Magnetization of 0-29 Ma ocean crust on the Mid-Atlantic Ridge, 25 degrees 30′ to 27 degrees 10′ N. *Journal of Geophysical Research*, *103*, 17,807–17,826. https://doi.org/10.1029/98JB01394

Wessel, P., & Smith, W. H. F. (1998). New, improved version of Generic Mapping Tools released. *Eos, Transactions of the American Geophysical Union*, *79*(47), 579. https://doi.org/10.1029/98EO00426

Xu, M., & Tivey, M. A. (2016). Investigation of a marine magnetic polarity reversal boundary in cross-section at the northern boundary of the Kane Megamullion, Mid-Atlantic Ridge 23°40′N. *Journal of Geophysical Research: Solid Earth*, *121*, 3161–3176. https://doi.org/10.1002/2016JB012928

Yeo, I., Searle, R. C., Achenbach, K., LeBas, T., & Murton, B. J. (2012). Eruptive hummocks, building blocks of the upper ocean crust. *Geology*, *40*(1), 91–94. https://doi.org/10.1130/G31892.1